Evidence for Unresolved γ-Ray Point Sources in the Inner Galaxy

Samuel K. Lee, Mariangela Lisanti, Benjamin R. Safdi, Tracy R. Slatyer, and Wei Xue

Phys. Rev. Lett. **116**, 051103 — Published 4 February 2016

DOI: 10.1103/PhysRevLett.116.051103

Evidence for Unresolved Gamma-Ray Point Sources in the Inner Galaxy

Samuel K. Lee,[1,2] Mariangela Lisanti,[3] Benjamin R. Safdi,[4] Tracy R. Slatyer,[4] and Wei Xue[4]

[1]*Princeton Center for Theoretical Science, Princeton University, Princeton, NJ 08544*
[2]*Broad Institute, Cambridge, MA 02142*
[3]*Department of Physics, Princeton University, Princeton, NJ 08544*
[4]*Center for Theoretical Physics, Massachusetts Institute of Technology, Cambridge, MA 02139*

(Dated: December 17, 2015)

We present a new method to characterize unresolved point sources (PSs), generalizing traditional template fits to account for non-Poissonian photon statistics. We apply this method to *Fermi* Large Area Telescope gamma-ray data to characterize PS populations at high latitudes and in the Inner Galaxy. We find that PSs (resolved and unresolved) account for ∼50% of the total extragalactic gamma-ray background in the energy range ∼1.9 to 11.9 GeV. Within 10° of the Galactic Center with $|b| \geq 2°$, we find that ∼5–10% of the flux can be accounted for by a population of unresolved PSs, distributed consistently with the observed ∼GeV gamma-ray excess in this region. The excess is fully absorbed by such a population, in preference to dark-matter annihilation. The inferred source population is dominated by near-threshold sources, which may be detectable in future searches.

Dark-matter (DM) annihilation in the Galactic halo can contribute to the flux of high-energy gamma rays detected by experiments such as the *Fermi* Large Area Telescope [1]. Currently, an excess of ∼GeV gamma rays has been observed by *Fermi* near the Galactic Center (GC) [2–16]. The signal extends ∼10° off the plane, is approximately spherically symmetric, and has an intensity profile that falls as $r^{-2\gamma}$ with $\gamma \approx 1.1$–1.4 [12, 14]. The morphology and energy spectrum of the signal is consistent with DM annihilation. There is some possible tension between the DM interpretation and other searches, especially in dwarf galaxies [17]; alternate explanations include a new population of millisecond pulsars (MSPs) [11, 18–26] or cosmic-ray injection [27, 28].

This Letter addresses the potential contribution of unresolved point sources (PSs) to the excess through the use of a new statistical method, called a non-Poissonian template fit (NPTF). Our approach is model-independent, in that we remain agnostic about the nature of the PSs. To verify the method, we use it to characterize unresolved gamma-ray PSs at high Galactic latitudes. These findings represent one of the most precise measurements of the contribution of PSs to the extragalactic gamma-ray background (EGB) and have important implications for characterizing its source components.

The main focus of this Letter is to use the NPTF to search for a population of unresolved gamma-ray PSs in the Inner Galaxy (IG) with a morphology consistent with that of the excess. We find that the NPTF strongly prefers a PS origin for the excess over a DM-like (smooth diffuse) origin. The Supplementary Material provides further details on the method, as well as additional cross-checks that support these conclusions.

This study analyzes the Extended Pass 7 Reprocessed *Fermi* data from ∼August 4, 2008 to ∼December 5, 2013 made available by [29]. A HEALPix [30] pixelization of the data with $nside = 128$ is used, corresponding to pixels ∼0.5° to a side. We emphasize that our study focuses on data in a single energy bin from 1.893–11.943 GeV and does not rely on or extract spectral information for the excess. The choice of this energy range keeps the signal-to-background ratio in the region of interest (ROI) high, maintains a sufficiently large number of photons over the full sky, and keeps the point-spread function relatively small and energy-independent.

The analysis utilizes the photon-count probability distribution in each pixel. In general, a given model for the gamma-ray flux, with parameters θ, predicts a probability $p_k^{(p)}(\theta)$ of observing k photons in a pixel p. Several source components, each modeled by a spatial template, can contribute photons in a pixel. To date, analyses using templates have assumed Poisson statistics for the photon-count distribution—specifically, that $p_k^{(p)}(\theta)$ is the Poisson probability to draw k counts with mean given by the sum of the template components in pixel p.

To account for unresolved PSs, the standard template-fitting procedure must be generalized to include non-Poissonian photon counts. In the NPTF procedure, $p_k^{(p)}(\theta)$ depends on a potentially pixel-dependent PS source-count function dN_p/dF. The source-count function determines the average number of PSs within pixel p that contribute photon flux between F and $F + dF$. In this work, the source-count function is assumed to follow a broken power law, $dN_p/dF \propto A_p F^{-n}$, with pixel-dependent normalization A_p and indices n_1 (n_2) above (below) the break F_b that are constant between pixels. For isotropically distributed PSs, A_p is constant between pixels. To model a population of PSs that mimics a DM annihilation signal, A_p must instead follow the DM annihilation template. Semi-analytic methods for calculating the $p_k^{(p)}(\theta)$ with a broken power law source-count function were developed in [31, 32].

We include templates for up to seven different components in the NPTF analysis: *(1)* diffuse background, assuming the *Fermi* `p6v11` diffuse model; *(2) Fermi* bubbles, assuming uniform emission within the bubbles [34];

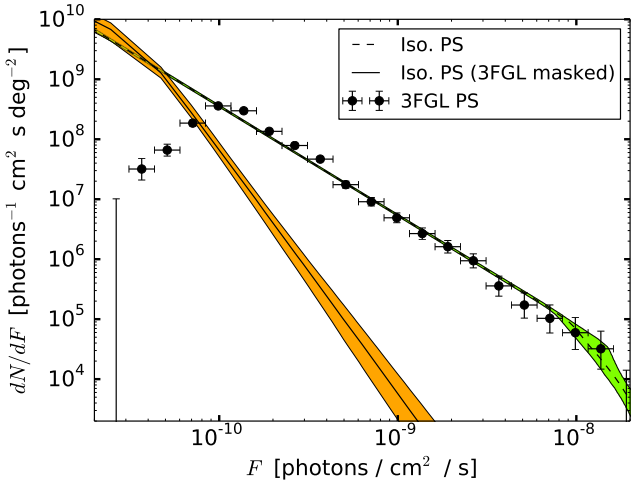

FIG. 1: The source-count function for high-latitude point sources, derived from applying non-Poissonian template fits to data with 3FGL sources [33] unmasked (green band) and masked (orange band). The colored bands indicate 68% confidence intervals, which are computed pointwise in F from the posteriors for the source-count–function parameters, while the solid and dashed black lines show the median source-count functions. The black points show the source-count function of the detected point sources in the 3FGL catalog. The vertical error bars indicate 68% confidence intervals; the horizontal bars denote bins in F.

(3) isotropic background; *(4)* annihilation of Navarro-Frenk-White (NFW) [35, 36]-distributed DM, assuming no substructure; *(5)* isotropic PSs; *(6)* disk-correlated PSs, and *(7)* NFW-distributed PSs.[1] Templates *(1)* through *(4)* are specified by a single normalization parameter each. Templates *(4)* and *(7)* assume a generalized NFW distribution with inner slope $\gamma = 1.25$. Template *(6)* corresponds to a doubly exponential thin-disk source distribution with scale height 0.3 kpc and radius 5 kpc. The PS templates each have four parameters describing their respective source-count functions.

Bayesian methods (implemented with `MultiNest` [37, 38]) are used to extract posterior distributions for the model parameters. The prior distributions of all parameters are flat, except for those of the DM and PS normalization factors, which are log flat. Unless otherwise stated, the prior ranges of all parameters are sufficiently large so that the posterior distribution is well-converged.

We begin by applying the NPTF to data at high Galactic latitudes ($|b| \geq 30^\circ$). *Fermi*'s third source catalog (3FGL) [33] identifies 1307 gamma-ray PSs in this region of the sky, with ∼55% associated with Active Galactic Nuclei and ∼24% associated with pulsars, supernova remnants and other known gamma-ray sources. The remaining ∼21% are unassociated. Figure 1 shows the source-count function dN/dF in terms of the flux of the 3FGL PSs in our energy bin (black points). The observed source-count function is suppressed below $F \sim 10^{-10}$ photons/cm^2/s, where it is hard to detect PSs over the diffuse background with the current exposure.

The NPTF is performed in this high-latitude region, including templates for the diffuse background, *Fermi* bubbles, isotropic emission, and isotropic PSs. The best-fit source-count function values are given in Tab. I.[2] The pointwise 68% confidence interval for the source-count function is shown in Fig. 1, shaded green. The source-count function matches the 3FGL data well above $F \sim 10^{-10}$ photons/cm^2/s.

The best-fit intensities obtained from the NPTF can be compared to those obtained from a standard template fit that neglects PSs. The diffuse-background and *Fermi*-bubbles intensities (averaged over the ROI) are consistent between both procedures. When the PS template is included, the isotropic-background intensity is $I_{\rm iso} = 1.38^{+0.07}_{-0.07} \times 10^{-7}$ photons/cm^2/s/sr and the isotropic PS intensity is $I^{\rm iso}_{\rm PS} = 1.67^{+0.08}_{-0.09} \times 10^{-7}$ photons/cm^2/s/sr. With no PS template, the isotropic-background intensity is over twice as high, $I_{\rm iso} = 3.00^{+0.03}_{-0.03} \times 10^{-7}$ photons/cm^2/s/sr. Thus, the PS intensity is absorbed by the isotropic-background template in the standard procedure.

The averaged intensity of the observed 3FGL PSs is $\sim 9.32 \times 10^{-8}$ photons/cm^2/s/sr at high latitudes. Using the result of the NPTF described above and neglecting systematic uncertainties in modeling the 3FGL PSs, we predict that the intensity of unresolved PSs is $7.38^{+0.83}_{-0.85} \times 10^{-8}$ photons/cm^2/s/sr. This can be checked explicitly by repeating the NPTF with all 3FGL PSs masked (at a ∼1° radius). The results of this fit are given in Tab. I and illustrated by the orange band in Fig. 1. The source-count function for the unresolved PSs agrees with that computed from the unmasked sky at low flux. This suggests that the NPTF is sensitive to contributions from unresolved PSs below *Fermi*'s detection threshold. The intensity of the isotropic background is $I_{\rm iso} = 1.55^{+0.07}_{-0.07} \times 10^{-7}$ photons/cm^2/s/sr, which agrees with that from the 3FGL-unmasked NPTF, within uncertainties. The intensity of the isotropic PSs is $I^{\rm iso}_{\rm PS} = 4.61^{+0.72}_{-0.88} \times 10^{-8}$ photons/cm^2/s/sr, which is slightly lower than the value inferred from the 3FGL-unmasked NPTF.

$I_{\rm iso}$ corresponds to the intensity of the isotropic

[1] More specifically, the 2-D spatial distribution of flux from the PSs, projected along the line-of-sight, follows the flux distribution of gamma-rays from DM annihilation, assuming the DM is distributed with a generalized NFW distribution.

[2] The exposure map in [29], with average exposure $\epsilon_{\rm avg} = 4.45 \times 10^{10}$ cm^2 s, is used to translate between the number of photons S and the flux F.

ROI	Template	3FGL	n_1	n_2	F_b [photons/cm^2/s]	Bayes Factor (Data)	Bayes Factor (Simulation)	NFW DM (95% confidence)
HL	Iso. PS	unmasked	$3.98^{+2.72}_{-0.72}$	$1.82^{+0.01}_{-0.02}$	$9.05^{+5.68}_{-2.06} \times 10^{-9}$	—	—	—
		masked	$4.06^{+0.40}_{-0.29}$	$1.56^{+0.12}_{-0.16}$	$3.72^{+1.40}_{-0.71} \times 10^{-12}$			
IG	NFW PS + Disk PS	unmasked	$18.2^{+8.44}_{-7.91}$	$-0.66^{+0.98}_{-0.90}$	$1.76^{+0.44}_{-0.35} \times 10^{-10}$	$\sim 10^6$	$\sim 10^5$	< 0.44 %
			$17.5^{+8.19}_{-8.40}$	$1.40^{+0.12}_{-0.15}$	$6.80^{+1.92}_{-1.25} \times 10^{-9}$			
IG	NFW PS + Disk PS	masked	$18.5^{+7.78}_{-8.09}$	$-0.73^{+1.07}_{-0.83}$	$1.62^{+0.45}_{-0.32} \times 10^{-10}$	$\sim 10^2$	$\sim 10^2$	< 0.48 %
			$17.0^{+8.85}_{-8.68}$	$-0.21^{+1.24}_{-1.18}$	$6.58^{+9.24}_{-4.36} \times 10^{-10}$			

TABLE I: Best-fit values (16^{th}, 50^{th}, and 84^{th} percentiles) for the source-count functions associated with the PS templates in the High Latitude (HL) and Inner Galaxy (IG) ROIs. The source-count function is fit by a broken power-law, where $n_{1(2)}$ is the slope above (below) the break in dN/dF, given by F_b. The source-count function for the isotropic PS component in the IG is not included, as its flux fraction is subdominant. Depending on the analysis, the *Fermi* 3FGL sources may either be masked or unmasked. Where appropriate, we provide the Bayes factor in preference for including the NFW PS component, in both the real data and in simulations, as well as the constraint on the flux fraction (calculated as in Fig. 2) attributed to NFW DM.

gamma-ray background (IGRB), while $I_{\rm iso}+I^{\rm iso}_{\rm PS}$ gives the intensity of the EGB. While the PS template does absorb some contribution from Galactic PSs, extragalactic PSs are expected to dominate. From the 3FGL-unmasked NPTF, we infer that 55^{+2}_{-2}% of the EGB in this energy range is associated with both resolved and unresolved PS emission; from the 3FGL-masked NPTF and using the intensities of the 3FGL PSs, we find that 47^{+2}_{-2}% of the EGB is due to PS emission. These estimates appear to be consistent with those in [31, 39], though a direct comparison is made difficult by the fact that these analyses cover a different energy range and only use the first $\sim$11 months of *Fermi* data. Our estimates for $I_{\rm iso}$ agree with the most recently published results from *Fermi* [40].

Next, we use the NPTF procedure to determine the fraction of flux from unresolved PSs in the IG. These analyses include templates for the diffuse background, the *Fermi* bubbles, isotropic background, and NFW-distributed DM, in addition to isotropic, disk-correlated, and NFW-distributed PSs. While the prior ranges for the isotropic, isotropic PS, *Fermi* bubbles, and diffuse background template parameters are not constrained by the high-latitude fit, restricting these parameters to their high-latitude values does not significantly affect the results.[3]

The ROI consists of all pixels within 30° of the GC with $|b| \geq 2°$, masking out the plane. As above, we perform two analyses, one on the full ROI and another with all 3FGL PSs masked. For both cases, the source-count functions and flux fractions are quoted with respect to the region within 10° of the GC and $|b| \geq 2°$, with no PSs masked. The source-count function of the Galactic and unassociated 3FGL PSs in the IG is given by the black points in the left panel of Fig. 2, with the number of PSs in each bin indicated. The majority ($\sim$90%) of these PSs are unassociated.

Consider, first, the case where the 3FGL sources in the IG are unmasked. The left panel of Fig. 2 shows the best-fit source-count function for the NFW PS (dashed, orange), isotropic PS (dotted, green), and disk PS (solid, blue) populations. The disk-correlated PS template accounts for the high-flux 3FGL sources. Below $F \sim 2\times10^{-10}$ photons/cm^2/s, the NFW PS template accounts for nearly all the PS emission; its source-count function has a steep cutoff just below the source sensitivity threshold. It is worth noting that there is no externally imposed threshold for the PS population in this case, as the 3FGL sources are not masked.

The most pressing question to address is whether the excess flux in the IG is better absorbed by the NFW PS or NFW DM template. The right panel of Fig. 2 shows the respective flux fractions, computed relative to the total photon count in the inner 10° region with $|b| \geq 2°$

[3] In particular, allowing the isotropic and isotropic PS template parameters to float allows the isotropic components to partly compensate for flaws in the other templates. Mismodeling that is roughly uniform across the relatively small IG ROI can be absorbed in this way. For example, if our disk-correlated PS template is more sharply peaked toward the Galactic plane than the true disk PS population, the isotropic PS template can pick up an additional positive contribution that absorbs the higher-latitude disk PSs. If our disk PS template is broader in latitude than the true disk PS population, a negative contribution to the isotropic PS template can help account for this. Thus the "isotropic" templates in the IG may in principle be either brighter or fainter than their high-latitude counterparts.

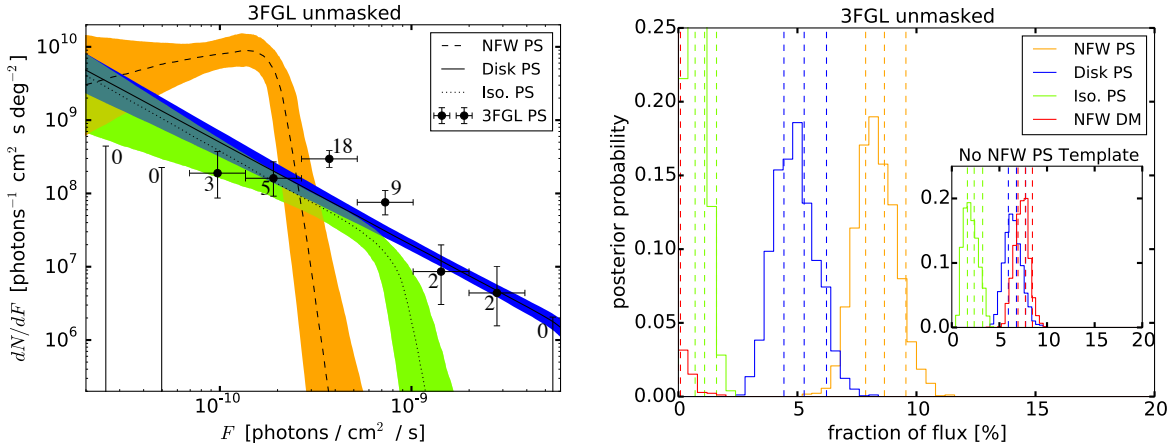

FIG. 2: (Left) Best-fit source-count functions within 10° of the GC and $|b| \geq 2°$, with the 3FGL sources unmasked. The median and 68% confidence intervals are shown for each of the following PS components: NFW (dashed, orange), thin-disk (solid, blue), and isotropic (dotted, green). The number of observed 3FGL sources in each bin is indicated. The normalization for the diffuse emission in the fit is consistent with that at high latitudes, as desired. (Right) Posteriors for the flux fraction within 10° of the GC with $|b| \geq 2°$ arising from the separate PS components, with 3FGL sources unmasked. The inset shows the result of removing the NFW PS template from the fit. Dashed vertical lines indicate the 16$^{\text{th}}$, 50$^{\text{th}}$, and 84$^{\text{th}}$ percentiles.

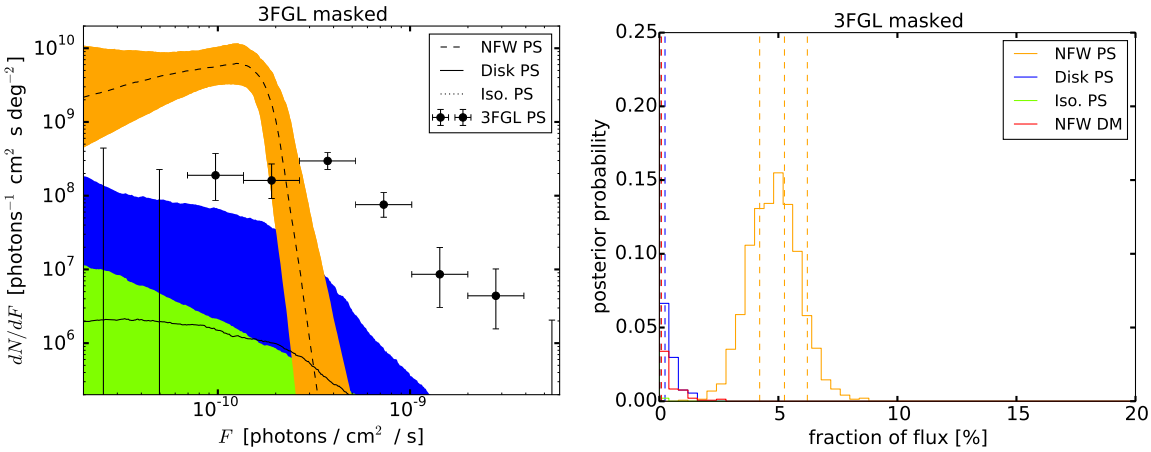

FIG. 3: Same as Fig. 2, except with 3FGL sources masked.

and the 3FGL sources unmasked. The disk and isotropic PSs contribute $5.3^{+0.9}_{-0.9}$% and $1.1^{+0.5}_{-0.4}$% of the flux, respectively. In contrast, the best-fit flux fraction for the NFW PS component is $8.7^{+0.9}_{-0.8}$%, while the best-fit DM flux fraction is consistent with zero. The normalization of the diffuse model remains consistent (to within 1%) with expectations from the fit at high latitudes, suggesting that the NFW PS template is absorbing the excess, and only the excess, and corresponds to a source population distinct from the more disk-like population of resolved sources. When the NFW PS template is omitted (inset), the fraction of flux absorbed by the disk PS population is essentially unchanged at $6.8^{+0.7}_{-0.9}$%, and the DM template absorbs $7.7^{+0.7}_{-0.8}$% of the flux. The DM flux obtained in absence of an NFW PS template is consistent with other estimates in the literature [12, 14]. The model including the NFW PS contribution is preferred over that without by a Bayes factor $\sim 10^6$.[4]

When the 3FGL sources are masked, the NPTF procedure yields a best-fit source-count function given by the orange band in the left panel of Fig. 3. Below the break, the source-count function agrees well with that found by the unmasked fit. In this case, the contributions from the isotropic and disk-correlated PS templates are negligible. The flux fraction attributed to the NFW PS component is $5.3^{+1.0}_{-1.1}$%, while the NFW DM template absorbs no significant flux.

In the masked analysis, the Bayes factor for a model that contains an NFW PS component, relative to one that does not, is $\sim 10^2$, substantially reduced relative to

[4] For reference, this corresponds to test statistic $2\Delta \ln \mathcal{L} \approx 36$.

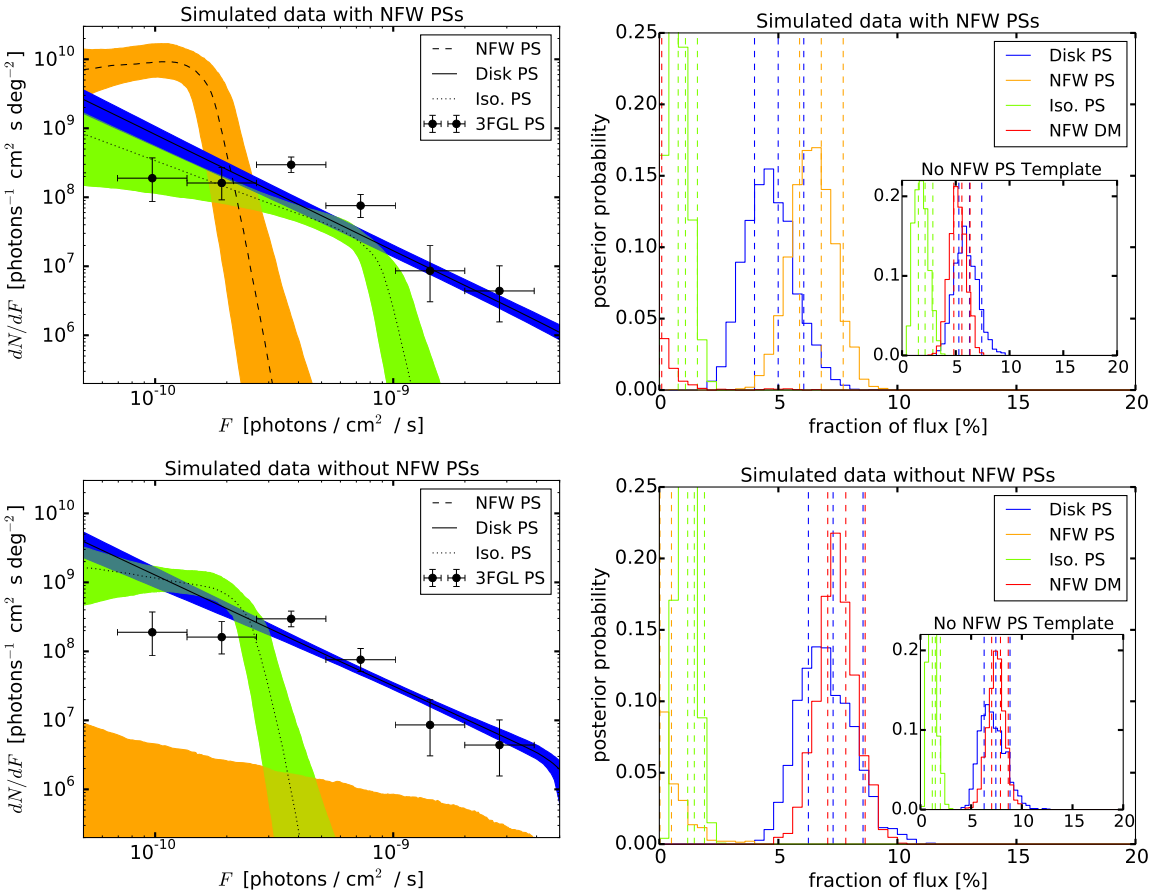

FIG. 4: Results obtained by applying the NPTF to simulated data. (Left column) The source-count functions for the PS templates in the fit when NFW PSs are included in the simulated data (top) or not (bottom). Note that when NFW PSs are not simulated, an NFW DM component is instead. (Right column) The associated posteriors for the fraction of flux absorbed by the different templates in the fit. The inset plots show the results of analyzing the simulated data without an NFW PS template in the fit. All plots are relative to the region within 10° of the GC with $|b| \geq 2°$ and 3FGL sources unmasked. For the flux-fraction plots, the fractions are computed relative to the total number of counts observed in the real data.

the result for the unmasked case. Masking the 3FGL sources removes most of the ROI within ∼5° of the GC, reducing photon statistics markedly, especially for any signal peaked at the GC. Furthermore, in the masked ROI, non-NFW PS templates can absorb a substantial fraction of the excess. For example, if only disk and isotropic PS templates are added, the flux fraction attributed to the disk template is $2.5^{+0.70}_{-0.62}$%, while that attributed to NFW DM is $2.2^{+1.6}_{-2.2}$% (the flux attributed to isotropic PSs is negligible). When no PS templates are included in the fit, the NFW DM template absorbs $4.1^{+1.1}_{-1.2}$% of the total flux. As we will discuss later, this behavior agrees with expectations from simulated data. In this statistics-limited regime, the fit does not distinguish different models for the PS distribution at high significance,[5] but there is still a strong preference for unresolved PSs. The Bayes factor for a model with disk and isotropic PSs, relative to one with no PSs, is ∼10^6, while the Bayes factor for a model with NFW, disk and isotropic PSs, relative to one with no PSs, is ∼10^8. The Bayes factors, best-fit source-count function parameters, and DM flux fractions for the 3FGL masked and unmasked analyses are summarized in Tab. I.

To validate the analysis procedure, we generate simulated data using the best-fit parameters from the unmasked IG analysis; we include isotropic, *Fermi* bubbles, and *Fermi* `p6v11` diffuse emission, as well as isotropic, disk and NFW-distributed PSs. The simulated data is then passed through the 3FGL-unmasked IG analysis

[5] However, if we repeat the analysis using Pass 8 data up to June 3, 2015, corresponding to an average exposure increase of ∼30% and a slight improvement in angular resolution, the Bayes factor in favor of NFW PSs increases from ∼10^2 to ∼10^4 in the 3FGL masked analysis; in the 3FGL unmasked analysis, the Bayes factor in favor of NFW PSs increases from ∼10^6 to ∼10^9.

pipeline described above. Details for how we perform the simulations may be found in the Supplementary Material.

The top row of Fig. 4 shows the source-count functions that are recovered from the NPTF (left), as well as the posterior distributions for the flux fractions of the separate components of the fit (right). The fitting procedure attributes the correct fraction of flux to NFW-distributed PSs, within uncertainties, and finds no evidence for NFW DM. When no NFW PS template is included in the fit (inset, top right), the NFW DM template absorbs the excess. Both the source-count functions and the flux fractions are consistent with the results obtained using real data. Additionally, we recover a Bayes factor of $\sim 10^5$ in preference for NFW PSs when using the simulated data, which is similar to what we found for the actual analysis.

For comparison, the bottom row of Fig. 4 shows the result of running the NPTF on a simulated data set that does not include NFW-distributed PSs but does include NFW DM. The model parameters used to generate the simulated data are taken from the best-fit values of the analysis without NFW PSs on the real data. In this case, the fitting procedure finds no evidence for NFW PSs, as it should, and the Bayes factor in preference for NFW PSs is much less than 1. The source-count functions recovered for disk-correlated and isotropic PSs are consistent with those used to generate the simulated data.

The source-count function that we recover for NFW PSs in the IG differs at low flux from those previously considered in the literature, which were motivated by population models and/or data for disk MSPs [19, 23, 24, 41]. In particular, our source-count function seems to prefer an increasing $dN/d\log F$ below the break, implying most sources lie close to the cutoff luminosity, while previously-considered source-count functions tend to be flatter or falling in $dN/d\log F$. If confirmed, this may suggest novel features of the source population; however, our results are also consistent with a flat or falling $dN/d\log F$ within uncertainties.

The results of the NPTF analyses presented here predict a new population of PSs directly below the PS-detection threshold in the IG. We estimate from the 3FGL unmasked (masked) analysis that half of the excess within 10° of the GC with $|b| \geq 2^\circ$ may be explained by a population of 132^{+31}_{-25} (86^{+32}_{-25}) unresolved PSs, with flux above $1.51^{+0.30}_{-0.25} \times 10^{-10}$ ($1.40^{+0.29}_{-0.27} \times 10^{-10}$) photons/cm^2/s. The entire excess within this region could be explained by 402^{+159}_{-91} (258^{+135}_{-83}) PSs, although this estimate relies on extrapolating the source-count function to very low flux, where systematic uncertainties are large. Detecting members of this PS population, which appears to lie just below the current *Fermi* PS-detection threshold, would be convincing evidence in favor of the PS explanation of the $\sim$GeV excess.

Acknowledgements.— We thank S. Ando, K. Blum, D. Caprioli, I. Cholis, C. Dvorkin, D. Finkbeiner, D. Hooper, M. Kaplinghat, T. Linden, S. Murgia, N. Rodd, J. Thaler, and N. Weiner for useful discussions. We thank the *Fermi* Collaboration for the use of *Fermi* public data and the Fermi Science Tools. B.R.S was supported by a Pappalardo Fellowship in Physics at MIT. This work is supported by the U.S. Department of Energy under grant Contract Numbers DE-SC00012567, DE-SC0013999 and DE-SC0007968. B.R.S. and T.R.S. thank the Aspen Center for Physics, which is supported by National Science Foundation grant PHY-1066293, for support during the completion of this work.

[1] W. Atwood et al. (Fermi-LAT), Astrophys.J. **697**, 1071 (2009).
[2] L. Goodenough and D. Hooper (2009), 0910.2998.
[3] D. Hooper and L. Goodenough, Phys.Lett. **B697**, 412 (2011).
[4] A. Boyarsky, D. Malyshev, and O. Ruchayskiy, Phys.Lett. **B705**, 165 (2011), 1012.5839.
[5] D. Hooper and T. Linden, Phys.Rev. **D84**, 123005 (2011), 1110.0006.
[6] K. N. Abazajian and M. Kaplinghat, Phys.Rev. **D86**, 083511 (2012), 1207.6047.
[7] D. Hooper and T. R. Slatyer, Phys.Dark Univ. **2**, 118 (2013), 1302.6589.
[8] C. Gordon and O. Macias, Phys.Rev. **D88**, 083521 (2013), 1306.5725.
[9] W.-C. Huang, A. Urbano, and W. Xue (2013), 1307.6862.
[10] O. Macias and C. Gordon, Phys.Rev. **D89**, 063515 (2014), 1312.6671.
[11] K. N. Abazajian et al., Phys.Rev. **D90**, 023526 (2014), 1402.4090.
[12] T. Daylan et al. (2014), 1402.6703.
[13] B. Zhou et al. (2014), 1406.6948.
[14] F. Calore, I. Cholis, and C. Weniger, JCAP **1403**, 038 (2015).
[15] K. N. Abazajian et al. (2014), 1410.6168.
[16] S. Murgia (Fermi-LAT) (Fermi Symposium, Nagoya, Japan, 2014).
[17] M. Ackermann et al. (Fermi-LAT) (2015), 1503.02641.
[18] K. N. Abazajian, JCAP **1103**, 010 (2011).
[19] D. Hooper et al., Phys.Rev. **D88**, 083009 (2013).
[20] N. Mirabal, Mon.Not.Roy.Astron.Soc. **436**, 2461 (2013), 1309.3428.
[21] Q. Yuan and B. Zhang, JHEAp **3-4**, 1 (2014).
[22] F. Calore et al., Astrophys.J. **796**, 1 (2014).
[23] I. Cholis, D. Hooper, and T. Linden (2014), 1407.5625.
[24] J. Petrovic, P. D. Serpico, and G. Zaharijas (2014), 1411.2980.
[25] Q. Yuan and K. Ioka (2014), 1411.4363.
[26] R. M. O'Leary et al. (2015), 1504.02477.
[27] E. Carlson and S. Profumo, Phys.Rev. **D90**, 023015 (2014).
[28] J. Petrovic, P. D. Serpico, and G. Zaharijas, JCAP **1410**, 052 (2014).
[29] S. K. Portillo and D. P. Finkbeiner, Astrophys.J. **796**, 54 (2014).
[30] K. Gorski et al., Astrophys.J. **622**, 759 (2005).
[31] D. Malyshev and D. W. Hogg, Astrophys.J. **738**, 181 (2011).
[32] S. K. Lee, M. Lisanti, and B. R. Safdi, JCAP **1505**, 056

(2015).
[33] F. Acero et al. (Fermi-LAT) (2015), 1501.02003.
[34] M. Su, T. R. Slatyer, and D. P. Finkbeiner, Astrophys.J. **724**, 1044 (2010).
[35] J. F. Navarro, C. S. Frenk, and S. D. White, Astrophys.J. **462**, 563 (1996).
[36] J. F. Navarro, C. S. Frenk, and S. D. White, Astrophys.J. **490**, 493 (1997).
[37] F. Feroz, M. Hobson, and M. Bridges, Mon.Not.Roy.Astron.Soc. **398**, 1601 (2009).
[38] J. Buchner et al., Astron.Astrophys. **564**, A125 (2014).
[39] A. A. Abdo et al. (Fermi-LAT), Astrophys. J. **720**, 435 (2010).
[40] M. Ackermann et al. (Fermi-LAT), Astrophys.J. **799**, 86 (2015).
[41] I. Cholis, D. Hooper, and T. Linden (2014), 1407.5583.
[42] A. Abdo et al. (Fermi-LAT), Astrophys.J.Suppl. **208**, 17 (2013).
[43] T. Grégoire and J. Knödlseder, Astron.Astrophys. **554**, A62 (2013).
[44] M. Ackermann et al. (Fermi-LAT), Astrophys.J. **750**, 3 (2012).